Ab initio Full Cell *GW*+DMFT for Correlated Materials

Tianyu Zhu* and Garnet Kin-Lic Chan†
Division of Chemistry and Chemical Engineering, California Institute of Technology, Pasadena CA 91125

Quantitative prediction of electronic properties in correlated materials requires simulations without empirical truncations and parameters. We present a method to achieve this goal through a new *ab initio* formulation of dynamical mean-field theory (DMFT). Instead of using small impurities defined in a low-energy subspace, which require complicated downfolded interactions which are often approximated, we describe a full cell *GW*+DMFT approach, where the impurities comprise all atoms in a unit cell or supercell of the crystal. Our formulation results in large impurity problems, which we treat here using an efficient coupled-cluster impurity solver that works on the real-frequency axis, combined with a one-shot G_0W_0 treatment of long-range interactions. We apply our full cell approach to bulk Si and two antiferromagnetic correlated insulators, NiO and α-Fe_2O_3, with impurities containing up to 10 atoms and 124 orbitals. We find that spectral properties, magnetic moments, and two-particle spin correlation functions are obtained in good agreement with experiments. In addition, in the metal oxides, the balanced treatment of correlations involving all orbitals in the cell leads to new insights into the orbital character around the insulating gap.

I. INTRODUCTION

Computing the properties of correlated electron materials with quantitative accuracy remains a fundamental challenge in *ab initio* simulations [1]. This is because strong electron interactions, for example in materials with open d or f shells, can lead to emergent phases such as high-temperature superconductivity, which cannot be described by the mean-field and low-order perturbation approximations commonly employed by *ab initio* methods.

Quantum embedding methods [2–5] in principle provide a promising route to access the phase diagrams of correlated materials, because they simultaneously treat strong local electron interactions and the thermodynamic limit. Among the different variants of quantum embedding used for this purpose, the combination of dynamical mean-field theory (DMFT) (and its cluster extensions [6, 7]) and density functional theory (DFT) [8], known as DFT+DMFT, is very popular [9–11]. In this combination, one views DFT as a low-level theory that accounts for band structure and the long-range interactions, while the high-level solution of the DMFT impurity problem, defined on a small set of correlated orbitals, introduces diagrams arising from the strong local interactions. Yet despite many successes, DFT+DMFT does not provide a truly parameter-free and quantitative *ab initio* theory of correlated materials, due to two closely related issues. First, the local Coulomb interaction in the DMFT impurity problem is typically treated as an adjustable Hubbard-like parameter [12], or is else estimated within another approximation [13]. Second, a double-counting correction [14, 15] is required to remove the DFT contribution to the local interactions, but no consistently accurate double-counting correction is known [16]. Beyond these two primary concerns arising from the local interactions, density functionals also do not always reliably account for the long-range interaction effects [17].

To obtain a truly quantitative, *ab initio* formulation of DMFT, one must work within a diagrammatically clean formalism. In this context, it is natural to replace DFT with the *GW* approximation [18] as the low-level theory. The *GW* approximation (often employed in its one-shot form (G_0W_0)) [19, 20] has been shown to fix many of the problems with semilocal density functionals (such as the underestimation of band gaps of weakly-correlated semiconductors) and thus appears a practical way to include the most important low-order long-range interaction diagrams. The combination with DMFT can then be formulated without double-counting by exactly subtracting the local *GW* contributions. The idea of self-consistently embedding the impurity self-energy and contributions to the polarization propagator arising from long-range interactions was proposed almost 17 years ago as the *GW*+(E)DMFT approximation [21, 22], but only very recently have self-consistent implementations appeared [23, 24]. However, while these developments are promising, applications have remained more limited than those with DFT+DMFT and have retained some problematic issues of that approach [25–28]. In particular, all current *GW*+(E)DMFT methods still require strongly downfolded interactions, because the impurity is restricted to the truncated low-energy subspace of a few correlated d or f orbitals (Fig. 1(b)). Downfolding to a small number of strongly coupled orbitals is numerically challenging, and yields retarded interactions that either limit the applicable impurity solvers or which must be truncated or otherwise approximated. If one ignores the embedding of the polarization propagator to work purely with the bare interactions, one obtains the self-energy embedding theory (SEET) [29]. However, applications of this simpler approach in solids also remain limited [30]. Aside from these technical issues, in some more complex correlated materials, the local orbitals can be intertwined with other itinerant bands [31, 32]. In such cases, even defining a set of local correlated orbitals can be difficult, and the quality of the calculation then depends sensitively on this choice [33].

A common origin of many of the above challenges is the definition of the impurity problem in terms of a small low-energy subspace. This is done only to obtain as simple an impurity problem as possible, as motivated by model Hamiltonians, but it is not a requirement of the more general DMFT

* tyzhu@caltech.edu
† gkc1000@gmail.com

formalism. Consequently, in this work, we present a new formulation, which we term *ab initio* full cell *GW*+DMFT. In this approach we define the impurity to be the full unit cell - or even multiple unit cells of atoms - where each atom is described by a large localized set of atomic orbitals, covering the core, valence and high-energy virtual orbitals (Fig. 1(a)). Since no low-energy subspace is identified, there is no downfolding, and we can simply use the full set of bare Coulomb interactions between the impurity orbitals, avoiding theoretical and numerical ambiguities. While conceptually simple, our full cell approach engenders two new complexities. The first is the need to set up the large impurity problem (for example to efficiently generate all the matrix elements) but this is enabled by technical advances we have made in the PySCF simulation platform [34] and our recently developed general *ab initio* quantum embedding framework [35, 36]. The second is the need to solve the resulting impurity problem with a large number of orbitals. Here, the key insight is that many orbitals in the full cell impurity are only weakly correlated, and impurity solvers which take advantage of this, such as those used in molecular quantum chemistry [37, 38] can then work very efficiently. In this work, we will use a coupled-cluster singles and doubles (CCSD) Green's function solver [39, 40] carrying out self-consistency along the real-frequency axis. We apply the full cell *GW*+DMFT method to compute the spectral properties of Si as well as the spectra, magnetic moments and spin correlation functions of two correlated insulators, NiO and α-Fe_2O_3, in their antiferromagnetic (AFM) phases. Our largest calculation in hematite uses an impurity of four Fe and six O atoms, giving rise to an unprecedentedly large *ab initio* DMFT impurity problem with 124 impurity orbitals.

II. THEORY AND IMPLEMENTATION

In the full cell *GW*+DMFT formulation, because the impurity cell contains all atoms in a crystal cell (or supercell), the effects of what would normally be thought of as long-range interactions on the polarization and self-energy from within the cell are all included. However, we will treat contributions from long-range interactions beyond the cell only at the level of the self-energy matrix of the crystal, computed at the one-shot G_0W_0 level. Because of this, certain contributions to the polarization propagator involving interactions far from the cell, that would require the bosonic self-consistency of EDMFT [41], are omitted. Our formulation is designed to capture the main effects of polarization on the local strongly correlated degrees of freedom, while avoiding the full cost of the bosonic (polarization) self-consistency loop.

Given a periodic crystal, we start by performing a one-shot G_0W_0 calculation on top of a mean-field reference (DFT or HF), using crystalline Gaussian atomic orbitals and Gaussian density fitting (GDF) integrals [42]. Because the G_0W_0 approximation is reference dependent, we will denote the approximation G_0W_0@reference. The full G_0W_0 self-energy matrix is computed in the mean-field molecular orbital (MO) basis along the imaginary-frequency axis [43, 44]:

$$\begin{aligned}\Sigma^{GW}_{nn'}(\mathbf{k}, i\omega) = &-\frac{1}{2\pi}\sum_{m\mathbf{k}_m}\int_{-\infty}^{\infty} d\omega' [\mathbf{G}_0(\mathbf{k}_m, i\omega - i\omega')]_{mm} \\ &\times \sum_{PQ\mathbf{k}_P} v_P^{nm}[\mathbf{I} - \mathbf{\Pi}(\mathbf{k}_P, i\omega')]^{-1}_{PQ} v_Q^{mn'},\end{aligned} \tag{1}$$

where v_P^{nm} represents the 3-index electron repulsion integral (ERI) $\left(P\mathbf{k}_P | n\mathbf{k}_n m\mathbf{k}_m\right)$, P is the Gaussian auxiliary basis, and n and m represent mean-field molecular orbitals (bands). $\mathbf{k}_P$, $\mathbf{k}_n$ and $\mathbf{k}_m$ satisfy crystal momentum conservation: $\mathbf{k}_P = \mathbf{k}_n - \mathbf{k}_m + n\mathbf{b}$, where $\mathbf{b}$ is a lattice vector, and $\mathbf{G}_0(\mathbf{k}_m, i\omega - i\omega')$ is the mean-field Green's function. The integration in Eq. 1 is carried out efficiently using a modified Gauss-Legendre grid [43] (100 grid points were used in this study). The polarization kernel $\mathbf{\Pi}(\mathbf{k}_P, i\omega')$ is

$$\mathbf{\Pi}_{PQ}(\mathbf{k}_P, i\omega') = 2\sum_{i\mathbf{k}_i}^{\text{occ}}\sum_{a\mathbf{k}_a}^{\text{vir}} v_P^{ia}\frac{\epsilon_{i\mathbf{k}_i} - \epsilon_{a\mathbf{k}_a}}{\omega'^2 + (\epsilon_{i\mathbf{k}_i} - \epsilon_{a\mathbf{k}_a})^2} v_Q^{ai}, \tag{2}$$

where $\epsilon_{i\mathbf{k}_i}$ and $\epsilon_{a\mathbf{k}_a}$ are occupied and virtual orbital energies respectively. Note that in a Gaussian basis formulation, the number of bands and size of auxiliary basis are significantly smaller than in plane-wave *GW* formulations [45], and because of this, the summations in Eqs. 1-2 run over all bands. To obtain the real-frequency G_0W_0 self-energy, we perform analytic continuation. Here, we fit the self-energy matrix elements to N-point Padé approximants ($N = 18$ in this work) using Thiele's reciprocal difference method [46]:

$$\Sigma^{GW}_{nn'}(\mathbf{k}, z) = \frac{a_0 + a_1\cdot z + \ldots + a_{(N-1)/2}\cdot z^{(N-1)/2}}{1 + b_1\cdot z + \ldots + b_{N/2}\cdot z^{N/2}}. \tag{3}$$

To define the impurity problem, we first construct an orthogonal atom-centered local orbital (LO) basis. As in our previous work on *ab initio* HF+DMFT and density matrix embedding theory (DMET), we employ crystalline intrinsic atomic orbitals (IAOs) and projected atomic orbitals (PAOs) as the local orthogonal basis [35, 36, 47]. IAOs are a set of valence atomic-like orbitals that exactly span the occupied space of the mean-field calculations, whose construction only requires projecting the DFT/HF orbitals onto predefined valence (minimal) AOs. PAOs, on the other hand, provide the remaining high-energy virtual atomic-like orbitals that complete the atomic basis and capture the correlation and screening effects.

The impurity consist of all LOs (i.e. all IAOs and PAOs) within the impurity cell (crystal cell or supercell) with IAOs representing the core and valence orbitals and PAOs representing the high-energy virtual orbitals. This is illustrated in Fig. 1(a). The most expensive step in forming the impurity Hamiltonian is computing the bare Coulomb interaction matrix $(ij|kl)$ for all orbitals within the impurity cell. However, using Gaussian density fitting, we can do this at relatively low cost (scaling asymptotically as $\mathcal{O}(N_{\mathbf{k}}^2 N_L N_{\text{AO}}^3)$, where $N_{\mathbf{k}}$, N_L and N_{AO} are the numbers of $\mathbf{k}$ points and auxiliary Gaussian and atomic orbitals within the impurity cell). We refer readers

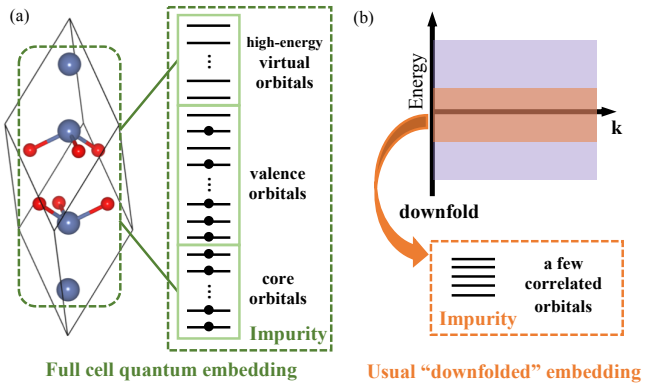

FIG. 1. Illustration of (a) *ab initio* full cell GW+DMFT and (b) usual GW+DMFT schemes. In full cell embedding, all orbitals in the full unit cell (four Fe and six O atoms) are taken as the impurity in the α-Fe_2O_3 calculation. In contrast, other GW+DMFT formulations define the impurity problem to contain a few correlated orbitals within a low-energy subspace which interact via downfolded, retarded, interactions.

to Ref. [36] for a detailed algorithm. The impurity Hamiltonian (without bath orbitals) is therefore

$$\hat{H}_{\rm imp} = \sum_{ij\in{\rm imp}} \tilde{F}_{ij} a_i^\dagger a_j + \frac{1}{2} \sum_{ijkl\in{\rm imp}} (ij|kl) a_i^\dagger a_k^\dagger a_l a_j, \quad (4)$$

with the one-particle interaction $\tilde{F}_{ij}$ defined as the Hartree-Fock effective Hamiltonian with the double-counting term subtracted

$$\tilde{F}_{ij} = (F_{\rm imp})_{ij} - \sum_{kl\in{\rm imp}} (\gamma_{\rm imp})_{kl} [(ij|lk) - \frac{1}{2}(ik|lj)], \quad (5)$$

and $\gamma_{\rm imp}$ is the impurity block of the mean-field density matrix.

We then start the DMFT cycle with an initial guess of the impurity self-energy as the G_0W_0 local self-energy: $\mathbf{\Sigma}_{\rm imp}(\omega) = \mathbf{\Sigma}^{GW}_{\rm DC}(\omega)$. The G_0W_0 local self-energy is computed in the LO basis within the impurity cell:

$$[\mathbf{\Sigma}^{GW}_{\rm DC}(i\omega)]_{ij} = -\frac{1}{2\pi} \sum_{kl} \int_{-\infty}^{\infty} d\omega' [\mathbf{G}_0^{\rm imp}(i\omega - i\omega')]_{kl} \times \sum_{RS} L_R^{ik} [\mathbf{I} - \mathbf{\Pi}(i\omega')]^{-1}_{RS} L_S^{lj}, \quad (6)$$

and analytically continued to the real axis. Here, all local orbital indices (i, j, k, l) are within the impurity cell. The 3-index tensor L_R^{ij} is computed from a Cholesky decomposition of the impurity ERI: $(ij|kl) = \sum_R L_R^{ij} L_R^{kl}$. Note that the polarization propagator is computed in the impurity orbital space, first in the imaginary time domain [48, 49]:

$$\mathbf{\Pi}_{RS}(\tau) = \sum_{ijkl\in{\rm imp}} L_P^{ij} [\mathbf{G}_0^{\rm imp}(\tau)]_{ki} L_Q^{kl} [\mathbf{G}_0^{\rm imp}(-\tau)]_{lj}, \quad (7)$$

and then cosine transformed into imaginary frequency space.

The hybridization self-energy is then computed:

$$\mathbf{\Delta}(\omega) = (\omega + \mu)\mathbf{I} - \mathbf{h}_{\rm imp} - \mathbf{\Sigma}_{\rm imp}(\omega) - \mathbf{G}^{-1}(\mathbf{R} = \mathbf{0}, \omega), \quad (8)$$

with the lattice Green's function defined as

$$\mathbf{G}(\mathbf{R} = \mathbf{0}, \omega) = \frac{1}{N_{\mathbf{k}}} \sum_{\mathbf{k}} [(\omega + \mu)\mathbf{I} - \mathbf{h}(\mathbf{k}) - \mathbf{\Sigma}(\mathbf{k}, \omega)]^{-1}, \quad (9)$$

and the full GW+DMFT self-energy defined as

$$\mathbf{\Sigma}(\mathbf{k}, \omega) = \mathbf{\Sigma}^{GW}(\mathbf{k}, \omega) + \mathbf{\Sigma}_{\rm imp}(\omega) - \mathbf{\Sigma}^{GW}_{\rm DC}(\omega). \quad (10)$$

Here, μ is the chemical potential, which is adjusted during the DMFT self-consistency to ensure that the electron count of the impurity is correct. $\mathbf{h}_{\rm imp}$ and $\mathbf{h}(\mathbf{k})$ are bare one-particle interactions for the impurity and whole solid.

In order to use a wavefunction (Hamiltonian-)based impurity solver, we discretize $\mathbf{\Delta}(\omega)$. We discretize along the real-frequency axis [50] so that dynamical quantities (e.g., spectral functions) are obtained more accurately. To obtain the discretization, we optimize bath couplings $\{V_{ip}^{(n)}\}$ and energies $\{\epsilon_n\}$ to minimize a cost function over a range of real-frequency points:

$$D = \sum_{\omega_l} \left\| \Delta_{ij}(\omega_l + i\eta) - \sum_{n=1}^{N_\epsilon} \sum_{p=1}^{N_p} \frac{V_{ip}^{(n)} V_{jp}^{(n)}}{\omega_l + i\eta - \epsilon_n} \right\|^2, \quad (11)$$

where N_ϵ is the number of bath energies and N_p is the number of bath orbitals per bath energy, and we use a broadening factor $\eta = 0.1$ a.u. . The bath degrees of freedom are truncated by only coupling bath orbitals to the valence IAOs, further reducing computational and optimization costs. The full embedding problem with both impurity and bath orbitals is thus defined from the Hamiltonian

$$\hat{H}_{\rm emb} = \hat{H}_{\rm imp} + \sum_{n=1}^{N_\epsilon} \sum_{p=1}^{N_p} \Big(\sum_i V_{ip}^{(n)} (a_i^\dagger a_{np} + a_{np}^\dagger a_i) + \epsilon_n a_{np}^\dagger a_{np} \Big). \quad (12)$$

We solve for the ground-state and Green's functions of the impurity Hamiltonian using a CCSD Green's function solver. At the singles and doubles level, CC may be viewed as generating ring, ladder, and coupled ring-ladder diagrams, and is known to be accurate in a variety of settings, including simple metallic and ordered magnetic states in *ab initio* calculations [51–53], and across weak to strong couplings when employed with small cluster DMFT impurities in Hubbard-like models [39]. (Note that the CCSD solver is certainly not the optimal solver for all problems, and other solvers will be explored in future work). From the CC Green's functions, we obtain an updated impurity self-energy $\mathbf{\Sigma}_{\rm imp}(\omega)$, and from this the DMFT cycle (Eqs. 8-12) is iterated until convergence between the impurity and lattice Green's functions:

$$\mathbf{G}_{\rm imp}(\omega) = \mathbf{G}(\mathbf{R} = \mathbf{0}, \omega). \quad (13)$$

III. RESULTS

We first apply our method to crystalline silicon. Although Si is considered a weakly-correlated semiconductor, it is still

a challenging system for many DFT functionals (such as LDA and GGA) which do not yield accurate band gaps [54]. One-shot G_0W_0 on top of LDA or GGA is known to significantly improve the band structure, although this relies somewhat on the cancellation of errors [55]. Such a small band-gap system also poses challenges to quantum embedding methods that start from a local correlation picture, such as DMFT [56], due to the long-range nature of its statically screened Coulomb interaction, which must be included in the treatment.

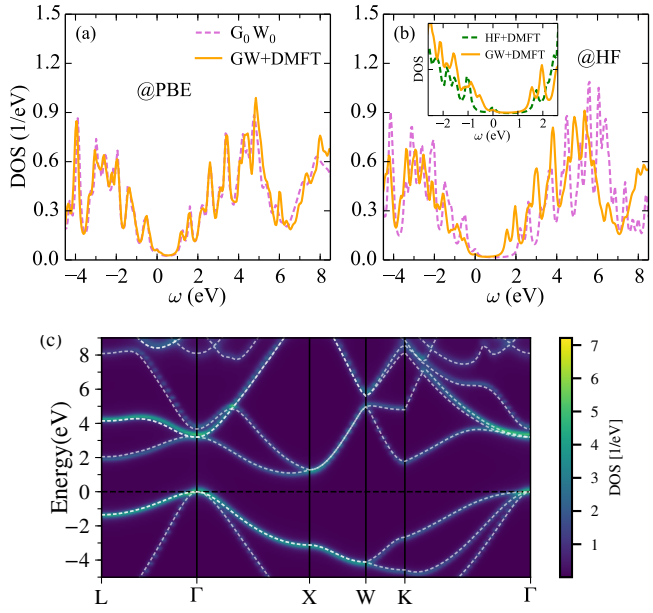

FIG. 2. Full cell GW+DMFT results for silicon. (a)(b) Local spectral function from GW+DMFT (PBE reference) and GW+DMFT (HF reference). Inset of (b): GW+DMFT compared to HF+DMFT ($4\times4\times4$ **k**-mesh and GTH-DZVP basis) DOS taken from Ref. [36]. (c) Band structure starting from PBE orbitals. The heat map represents the GW+DMFT@PBE result and the dashed line gives the G_0W_0 bands. A broadening factor of 0.1 eV is used.

The full cell GW+DMFT results for Si are presented in Fig. 2. We used the GTH-PADE pseudopotential [57] and GTH-TZVP basis [58], and a $6\times6\times6$ Γ-centered **k**-point sampling. The impurity was defined as the unit cell of 2 Si atoms with 34 local orbitals ($2s2p3s3p3d4s4p$ for Si), and 128 bath orbitals were used. As known from other G_0W_0 calculations [59] and as seen in Figs. 2(a) and 2(b), the mean-field starting point strongly affects the quality of the G_0W_0 results; G_0W_0@PBE gives an accurate band gap of 1.09 eV when compared to the experimental value of 1.17 eV [60], while G_0W_0@HF overestimates the band gap, giving 2.04 eV. GW+DMFT predicts the band gap of Si to be 1.01 eV (@PBE) and 1.39 eV (@HF), largely removing the reference dependence of G_0W_0, due to the more complete inclusion of diagrams from interactions within the unit cell. The spectral function is also greatly improved in GW+DMFT compared to G_0W_0@HF. In earlier HF+DMFT calculations [36] (see inset of Fig. 2(b)), we found the band gap to be too large by 0.5 eV, and this quantifies the effect of the long-range correlations in G_0W_0 on the band gap of Si. From Fig. 2(c), we note that GW+DMFT@PBE maintains the accurate band structure of G_0W_0@PBE, in contrast to self-consistent GW, which is known to lead to worse results than G_0W_0 itself [61, 62].

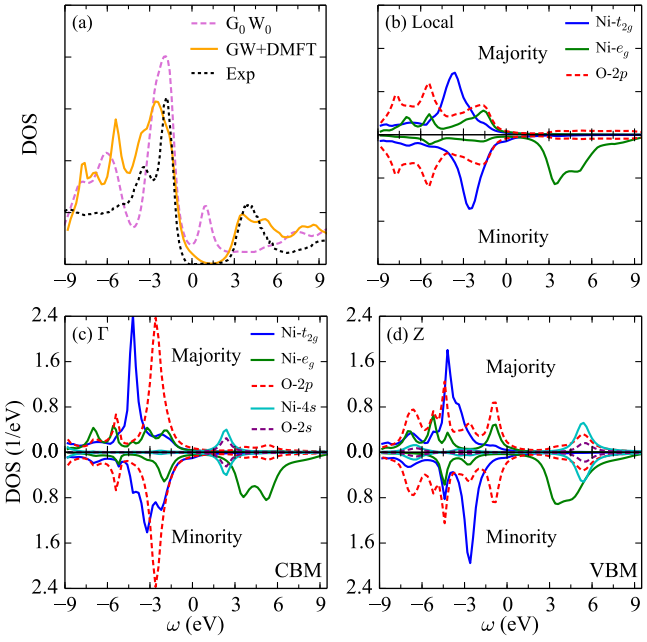

FIG. 3. Full cell GW+DMFT results for NiO (AFM phase) based on the PBE reference. (a) Local DOS. (b) Orbital-resolved local DOS. (c)(d) Orbital-resolved and momentum-resolved DOS at the Γ point (CBM) and Z = (0.5, 0.5, 0.5) point (VBM). A broadening factor of 0.4 eV is used.

We next show the results of full cell GW+DMFT in Fig. 3 for a strongly-correlated insulator, NiO, in the antiferromagnetic phase. The GTH-PADE pseudopotential and GTH-DZVP-MOLOPT-SR basis set [63] were used with a $6\times6\times6$ Γ-centered **k**-point sampling defined with respect to the antiferromagnetic cell (2 NiO units). (As an estimate of the remaining finite size error, the difference between the G_0W_0@PBE gaps for $4\times4\times4$ and $6\times6\times6$ **k**-meshes is only 0.1 eV). We used the antiferromagnetic cell of 2 NiO units along the [111] direction as the impurity, corresponding to 78 impurity orbitals ($3s3p3d4s4p4d4f$ for Ni and $2s2p3s3p3d$ for O) and 72 bath orbitals in the DMFT impurity problem. As seen in Fig. 3(a), G_0W_0@PBE severely underestimates the band gap at 1.9 eV, even when using a spin symmetry broken PBE reference. Meanwhile, the valence spectrum of G_0W_0@PBE does not agree well with the experimental photoemission spectrum [64]. GW+DMFT, on the other hand, predicts a band gap of 4.0 eV and a magnetic moment of 1.69 μ_B, both in very good agreement with the experimental values of 4.3 eV [64] and 1.77-1.90 μ_B [65, 66]. More interestingly, our GW+DMFT DOS captures the experimental two-peak structure of the valence spectrum around -2 and -3 eV. A detailed analysis of the spin-orbital-resolved local DOS in Fig. 3(b) reveals that this two-peak structure results from the splitting of the majority and minority spin components of the Ni-t_{2g} orbitals, and is a signature of the AFM phase, as it does

not arise within the paramagnetic phase [67]. From the local DOS, we can also conclude that NiO is an insulator with mixed charge-transfer and Mott character, with a valence band with contributions from Ni-t_{2g}, Ni-e_g and O-2p, and a conduction band that is mainly of Ni-e_g character.

In Figs. 3(c) and 3(d), we further analyze the character of the conduction band minimum (CBM) and valence band maximum (VBM) in the Brillouin zone using the momentum-resolved DOS. We find that the lowest conduction band has strong Ni-4s and O-2s character at the Γ point (CBM), which was not discussed in many earlier DMFT calculations [28, 68, 69] which focused on the Ni-3d and O-2p orbitals and thus did not include Ni-4s (or O-2s) orbitals in the impurity (although see Ref. [70] for a notable exception), unlike our full cell GW+DMFT treatment. At the Z point (VBM), we find that the highest valence band has significant O-2p and Ni-e_g contributions, with very little Ni-t_{2g} character. This is very different from the local DOS, where the Ni-t_{2g} has dominant weight in the valence bands. We confirm this by plotting the spatially-resolved DOS of NiO in the (001) plane in Fig. 4. We see that at the first valence peak and around the Ni atoms, the local spatial DOS has a Ni-t_{2g} (d_{xy}) orbital shape, while the momentum-resolved spatial DOS (at the Z point) has a Ni-e_g ($d_{x^2-y^2}$) orbital shape. Further, the weight of the DOS around the O atoms in Fig. 4(b) is considerably larger than in Fig. 4(a).

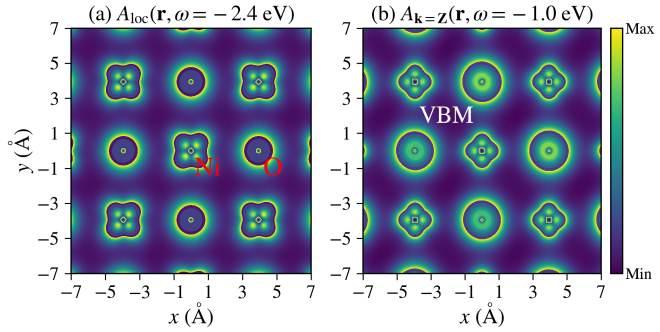

FIG. 4. Spatially-resolved DOS from GW+DMFT (PBE reference) for NiO in the (001) plane. (a) Local DOS at $\omega = -2.4$ eV. (b) Momentum-resolved DOS at VBM energy $\omega = -1.0$ eV and Z = (0.5, 0.5, 0.5) point.

Since our impurity includes two NiO units, we can also look at correlations across the cells. We computed the spin-spin correlation function for the Ni atoms within the impurity problem:

$$\sum_{i\in \mathrm{Ni}_1, j\in \mathrm{Ni}_2} \langle \mathbf{S}_i \cdot \mathbf{S}_j \rangle = \sum_{i\in \mathrm{Ni}_1, j\in \mathrm{Ni}_2} \sum_{a=x,y,z} \langle S_i^a S_j^a \rangle. \qquad (14)$$

We found $\langle \mathbf{S}_i \cdot \mathbf{S}_j \rangle$ between two Ni atoms to be -0.707. Both $\langle S_i^x S_j^x \rangle$ and $\langle S_i^y S_j^y \rangle$ contribute almost zero spin correlation, and the uncorrelated value $\langle S_i^z \rangle \langle S_j^z \rangle$ is -0.710, suggesting that quantum spin correlations are weak and NiO is close to a classical Ising magnet. This is consistent with experimental measurements of the critical behavior of the magnetic phase transition in NiO [71] and our previous *ab initio* DMET study [35].

We next turn to study a second strongly-correlated insulator, hematite (α-Fe_2O_3), in the AFM phase. We take the impurity to be the complete AFM unit cell, including 2 Fe_2O_3 units (Fig. 1), with a "+ − +−" type AFM ordering of the Fe spins. Because of the large impurity size, we used a DZV-quality basis (GTH-DZV-MOLOPT-SR, 3s3p3d4s4p4d5s for Fe, 2s2p3s3p for O), leading to an impurity problem with 124 impurity and 48 bath orbitals. The small number of bath orbitals is due to the current numerical limitations of our CCSD solver. However, since our bath orbitals are only coupled to the valence impurity orbitals, and we aim to reproduce the hybridization only in a window near the Fermi surface (±0.4 a.u.), the bath discretization error is not too severe. The 3s3p orbitals of Fe were treated as frozen core orbitals (i.e., uncorrelated) in the CCSD solver. The GTH-PBE pseudopotential and 4 × 4 × 4 Γ-centered **k**-point sampling were employed. As presented in Fig. 5(a), G_0W_0@PBE severely underestimates the band gap at 0.5 eV, compared to the experimental value of 2.6 eV [72]. G_0W_0 with the hybrid functional PBE0 slightly overestimates the gap (3.4 eV), but the spectrum does not agree well with experiment, and in particular, the features of the G_0W_0@PBE0 DOS are too sharp around -7 and 3.5 eV (Fig. 5(b)).

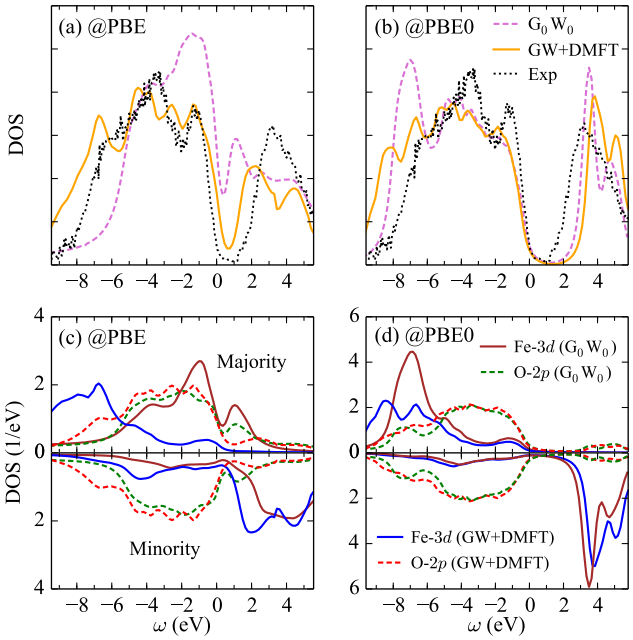

FIG. 5. Full cell GW+DMFT results for α-Fe_2O_3 (AFM phase). (a)(b) Local DOS based on PBE and PBE0 references. (c)(d) Orbital-resolved DOS corresponding to (a)(b). A broadening factor of 0.3 eV is used.

GW+DMFT improves the G_0W_0@PBE spectrum significantly, especially in the valence region, although the band gap (1.5 eV) is still too small. From the orbital-resolved DOS in Fig. 5(c), we find that the main improvement comes from the spectral positions of the majority spin component of the Fe-3d orbitals and O-2p orbitals. G_0W_0@PBE mistakenly predicts the Fe-3d valence spectrum to lie close to the Fermi surface and that Fe_2O_3 has considerable Mott insulating character. However, GW+DMFT shifts the majority-spin Fe-3d

DOS to lower energies, consistent with previous DFT+DMFT calculations [73, 74]. Because of this correction, GW+DMFT obtains a more accurate Fe magnetic moment than PBE (4.23 μ_B compared to 3.71 μ_B with the experimental moment being 4.64 μ_B [75]). We find that the valence band spectrum is dominated by O-2p near the Fermi surface, indicating that Fe_2O_3 is in fact a pure charge-transfer insulator, with almost no Mott insulating character. This is in contrast to DFT+DMFT calculations [73, 74] that find a sizable Fe-3d contribution to the valence band maximum. We attribute this disagreement to the full cell GW+DMFT treatment where both O-2p orbitals and Fe-3d are treated on an equal footing at the impurity level, which thus allows for a more accurate balancing of their relative contributions to the spectral weight.

Starting from a PBE0 reference, GW+DMFT finds a slightly larger band gap (3.9 eV) and magnetic moment (4.37 μ_B) than G_0W_0 (3.4 eV and 4.20 μ_B). The overly sharp peaks of the G_0W_0@PBE0 spectrum around -7 and 3.5 eV are corrected by GW+DMFT, which broadens the Fe-3d peaks as shown in Fig. 5(d). In summary, it appears we achieve a good description of the photoemission spectrum for Fe_2O_3 within the full cell GW+DMFT, although a fully quantitative prediction of the band gap is not attained. Given that G_0W_0 only provides a minor correction to the underlying DFT band gap in this system, the likely culprit is the insufficiency of the G_0W_0 approximation in describing the long-range interactions in Fe_2O_3.

IV. CONCLUSIONS

In this work, we introduced a full cell GW+DMFT formulation for the *ab initio* simulation of correlated materials. The primary strength of this approach is that it entirely avoids the problem of selecting a low-energy subspace, and consequently the uncontrolled errors introduced either by downfolding the effective interactions within the subspace, or via DFT double counting. The resulting method is then both parameter free and can easily treat all interactions. We showed that full cell GW+DMFT can be applied to systems using impurity cells of up to 10 atoms in calculations of the spectral properties of Si, NiO and α-Fe_2O_3, obtaining for most quantities, results of good quantitative accuracy. By defining the impurity to comprise all orbitals in the AFM supercells of NiO and α-Fe_2O_3, we also showed how the full cell approach can cleanly differentiate between different amounts of charge-transfer and Mott insulating character and the orbital character around the gap, as both metal and non-metal orbitals enter into the impurity problem on an equal footing. Overall, our calculations demonstrate the potential of the full cell GW+DMFT approach for studies of more complicated materials, en route towards a fully predictive theory of correlated materials.

ACKNOWLEDGMENTS

This work was supported by the US Department of Energy via the M^2QM EFRC under award no. de-sc0019330. TZ thanks helpful discussions from Zhihao Cui, Xing Zhang and Timothy Berkelbach. Additional support was provided by the Simons Foundation via the Simons Collaboration on the Many Electron Problem, and via the Simons Investigatorship in Physics.

[1] P. R. Kent and G. Kotliar, Science **361**, 348 (2018).
[2] A. Georges and G. Kotliar, Phys. Rev. B **45**, 6479 (1992).
[3] A. Georges, G. Kotliar, W. Krauth, and M. Rozenberg, Rev. Mod. Phys. **68**, 13 (1996).
[4] G. Knizia and G. K.-L. Chan, Phys. Rev. Lett. **109**, 186404 (2012).
[5] Q. Sun and G. K.-L. Chan, Acc. Chem. Res. **49**, 2705 (2016), arXiv:1612.02576.
[6] G. Kotliar, S. Y. Savrasov, G. Pálsson, and G. Biroli, Phys. Rev. Lett. **87**, 186401 (2001), arXiv:0010328 [cond-mat].
[7] M. Hettler, M. Mukherjee, M. Jarrell, and H. Krishnamurthy, Phys. Rev. B **61**, 12739 (2000).
[8] W. Kohn and L. J. Sham, Phys. Rev. **140**, A1133 (1965).
[9] K. Held, I. A. Nekrasov, G. Keller, V. Eyert, N. Blümer, A. K. McMahan, R. T. Scalettar, T. Pruschke, V. I. Anisimov, and D. Vollhardt, Phys. status solidi **243**, 2599 (2006).
[10] G. Kotliar, S. Y. Savrasov, K. Haule, V. S. Oudovenko, O. Parcollet, and C. A. Marianetti, Rev. Mod. Phys. **78**, 865 (2006).
[11] K. Held, Adv. Phys. **56**, 829 (2007).
[12] F. Nilsson and F. Aryasetiawan, Computation **6**, 26 (2018).
[13] F. Aryasetiawan, M. Imada, A. Georges, G. Kotliar, S. Biermann, and A. I. Lichtenstein, Phys. Rev. B **70**, 195104 (2004).
[14] X. Wang, M. J. Han, L. de' Medici, H. Park, C. A. Marianetti, and A. J. Millis, Phys. Rev. B **86**, 195136 (2012).
[15] K. Haule, Phys. Rev. Lett. **115**, 196403 (2015).
[16] M. Karolak, G. Ulm, T. Wehling, V. Mazurenko, A. Poteryaev, and A. Lichtenstein, J. Electron Spectros. Relat. Phenom. **181**, 11 (2010).
[17] J. P. Perdew, W. Yang, K. Burke, Z. Yang, E. K. Gross, M. Scheffler, G. E. Scuseria, T. M. Henderson, I. Y. Zhang, A. Ruzsinszky, H. Peng, J. Sun, E. Trushin, and A. Görling, Proc. Natl. Acad. Sci. U. S. A. **114**, 2801 (2017).
[18] L. Hedin, Phys. Rev. **139**, A796 (1965).
[19] M. S. Hybertsen and S. G. Louie, Phys. Rev. B **34**, 5390 (1986).
[20] M. Shishkin and G. Kresse, Phys. Rev. B **74**, 035101 (2006).
[21] P. Sun and G. Kotliar, Phys. Rev. B **66**, 085120 (2002).
[22] S. Biermann, F. Aryasetiawan, and A. Georges, Phys. Rev. Lett. **90**, 086402 (2003).
[23] L. Boehnke, F. Nilsson, F. Aryasetiawan, and P. Werner, Phys. Rev. B **94**, 201106 (2016).
[24] S. Choi, P. Semon, B. Kang, A. Kutepov, and G. Kotliar, Comput. Phys. Commun. **244**, 277 (2019), arXiv:1810.01679.
[25] J. M. Tomczak, M. Casula, T. Miyake, F. Aryasetiawan, and S. Biermann, EPL **100**, 67001 (2012), arXiv:1210.6580.

[26] C. Taranto, M. Kaltak, N. Parragh, G. Sangiovanni, G. Kresse, A. Toschi, and K. Held, Phys. Rev. B **88**, 165119 (2013), arXiv:1211.1324.

[27] J. Tomczak, P. Liu, A. Toschi, G. Kresse, and K. Held, Eur. Phys. J. Spec. Top. **226**, 2565 (2017).

[28] S. Choi, A. Kutepov, K. Haule, M. van Schilfgaarde, and G. Kotliar, npj Quantum Mater. **1**, 16001 (2016).

[29] T. N. Lan, A. Shee, J. Li, E. Gull, and D. Zgid, Phys. Rev. B **96**, 155106 (2017).

[30] A. A. Rusakov, S. Iskakov, L. N. Tran, and D. Zgid, J. Chem. Theory Comput. **15**, 229 (2019).

[31] D. H. Lu, M. Yi, S. K. Mo, A. S. Erickson, J. Analytis, J. H. Chu, D. J. Singh, Z. Hussain, T. H. Geballe, I. R. Fisher, and Z. X. Shen, Nature **455**, 81 (2008).

[32] C. Weber, K. Haule, and G. Kotliar, Nat. Phys. **6**, 574 (2010), arXiv:1005.3095.

[33] B. Amadon, F. Lechermann, A. Georges, F. Jollet, T. O. Wehling, and A. I. Lichtenstein, Phys. Rev. B **77**, 205112 (2008).

[34] Q. Sun, T. C. Berkelbach, N. S. Blunt, G. H. Booth, S. Guo, Z. Li, J. Liu, J. D. McClain, E. R. Sayfutyarova, S. Sharma, S. Wouters, and G. K.-L. Chan, Wiley Interdiscip. Rev. Comput. Mol. Sci. **8**, e1340 (2018).

[35] Z. H. Cui, T. Zhu, and G. K.-L. Chan, J. Chem. Theory Comput. **16**, 119 (2020), arXiv:1909.08596.

[36] T. Zhu, Z.-H. Cui, and G. K.-L. Chan, J. Chem. Theory Comput. **16**, 141 (2020).

[37] D. Zgid and G. K.-L. Chan, J. Chem. Phys. **134**, 094115 (2011).

[38] D. Zgid, E. Gull, and G. K. L. Chan, Phys. Rev. B **86**, 1 (2012), arXiv:1203.1914.

[39] T. Zhu, C. A. Jiménez-Hoyos, J. McClain, T. C. Berkelbach, and G. K.-L. Chan, Phys. Rev. B **100**, 115154 (2019).

[40] A. Shee and D. Zgid, J. Chem. Theory Comput. **15**, 6010 (2019).

[41] F. Nilsson, L. Boehnke, P. Werner, and F. Aryasetiawan, Phys. Rev. Mater. **1**, 043803 (2017), arXiv:1706.06808.

[42] Q. Sun, T. C. Berkelbach, J. D. McClain, and G. K.-L. Chan, J. Chem. Phys. **147**, 164119 (2017).

[43] X. Ren, P. Rinke, V. Blum, J. Wieferink, A. Tkatchenko, A. Sanfilippo, K. Reuter, and M. Scheffler, New J. Phys. **14**, 053020 (2012), arXiv:1201.0655.

[44] J. Wilhelm, M. Del Ben, and J. Hutter, J. Chem. Theory Comput. **12**, 3623 (2016).

[45] G. H. Booth, T. Tsatsoulis, G. K. L. Chan, and A. Grüneis, J. Chem. Phys. **145**, 084111 (2016), arXiv:1603.06457.

[46] H. J. Vidberg and J. W. Serene, J. Low Temp. Phys. **29**, 179 (1977).

[47] G. Knizia, J. Chem. Theory Comput. **9**, 4834 (2013).

[48] P. Liu, M. Kaltak, J. Klimeš, and G. Kresse, Phys. Rev. B **94**, 165109 (2016), arXiv:1607.02859.

[49] J. Wilhelm, D. Golze, L. Talirz, J. Hutter, and C. A. Pignedoli, J. Phys. Chem. Lett. **9**, 306 (2018).

[50] I. de Vega, U. Schollwöck, and F. A. Wolf, Phys. Rev. B **92**, 155126 (2015).

[51] J. McClain, J. Lischner, T. Watson, D. A. Matthews, E. Ronca, S. G. Louie, T. C. Berkelbach, and G. K.-L. Chan, Phys. Rev. B **93**, 235139 (2016).

[52] Y. Gao, Q. Sun, J. M. Yu, M. Motta, J. McClain, A. F. White, A. J. Minnich, and G. K.-L. Chan, arXiv:1910.02191 (2019), arXiv:1910.02191.

[53] K. T. Williams, Y. Yao, J. Li, L. Chen, H. Shi, M. Motta, C. Niu, U. Ray, S. Guo, R. J. Anderson, J. Li, L. N. Tran, C.-N. Yeh, B. Mussard, S. Sharma, F. Bruneval, M. van Schilfgaarde, G. H. Booth, G. K.-L. Chan, S. Zhang, E. Gull, D. Zgid, A. Millis, C. J. Umrigar, and L. K. Wagner, Phys. Rev. X **10**, 011041 (2020).

[54] J. Heyd, J. E. Peralta, G. E. Scuseria, and R. L. Martin, J. Chem. Phys **123**, 174101 (2005).

[55] M. Shishkin, M. Marsman, and G. Kresse, Phys. Rev. Lett. **99**, 246403 (2007).

[56] N. E. Zein, S. Y. Savrasov, and G. Kotliar, Phys. Rev. Lett. **96**, 226403 (2006).

[57] C. Hartwigsen, S. Goedecker, and J. Hutter, Phys. Rev. B **58**, 3641 (1998).

[58] J. Vandevondele, M. Krack, F. Mohamed, M. Parrinello, T. Chassaing, and J. Hutter, Comput. Phys. Commun. **167**, 103 (2005).

[59] F. Fuchs, J. Furthmüller, F. Bechstedt, M. Shishkin, and G. Kresse, Phys. Rev. B **76**, 115109 (2007), arXiv:0604447 [cond-mat].

[60] K. P. O'Donnell and X. Chen, Appl. Phys. Lett. **58**, 2924 (1991).

[61] M. Shishkin and G. Kresse, Phys. Rev. B **75**, 235102 (2007).

[62] A. L. Kutepov, Phys. Rev. B **95**, 195120 (2017).

[63] J. VandeVondele and J. Hutter, J. Chem. Phys. **127**, 114105 (2007).

[64] G. A. Sawatzky and J. W. Allen, Phys. Rev. Lett. **53**, 2339 (1984).

[65] B. E. F. Fender, A. J. Jacobson, and F. A. Wedgwood, J. Chem. Phys. **48**, 990 (1968).

[66] A. K. Cheetham and D. A. O. Hope, Phys. Rev. B **27**, 6964 (1983).

[67] B. Kang and S. Choi, arXiv:1908.05643 (2019), arXiv:1908.05643.

[68] J. Kuneš, V. I. Anisimov, S. L. Skornyakov, A. V. Lukoyanov, and D. Vollhardt, Phys. Rev. Lett. **99**, 156404 (2007).

[69] I. Leonov, L. Pourovskii, A. Georges, and I. A. Abrikosov, Phys. Rev. B **94**, 155135 (2016), arXiv:1607.08261.

[70] L. Zhang, P. Staar, A. Kozhevnikov, Y. P. Wang, J. Trinastic, T. Schulthess, and H. P. Cheng, Phys. Rev. B **100**, 035104 (2019), arXiv:1705.02387.

[71] T. Chatterji, G. J. McIntyre, and P. A. Lindgard, Phys. Rev. B **79**, 172403 (2009).

[72] R. Zimmermann, P. Steiner, R. Claessen, F. Reinert, S. Hüfner, P. Blaha, and P. Dufek, J. Phys. Condens. Matter **11**, 1657 (1999).

[73] J. Kuneš, D. M. Korotin, M. A. Korotin, V. I. Anisimov, and P. Werner, Phys. Rev. Lett. **102**, 146402 (2009).

[74] E. Greenberg, I. Leonov, S. Layek, Z. Konopkova, M. P. Pasternak, L. Dubrovinsky, R. Jeanloz, I. A. Abrikosov, and G. K. Rozenberg, Phys. Rev. X **8**, 031059 (2018).

[75] J. M. Coey and G. A. Sawatzky, J. Phys. C Solid State Phys. **4**, 2386 (1971).